Available online at www.HighTechJournal.org

HighTech and Innovation Journal

ISSN: 2723-9535

Vol. 7, No. 2, June, 2026

# Performance Analysis of a Cross-Flow Turbine Runner Made of HDPE-Wood Fiber Biocomposite

Francis M. Kifumbi [1*], Guyh D. Ngoma [1], Fouad Erchiqui [1], Theophile M. Tshibangu [1]

[1] *School of Engineering, University of Quebec in Abitibi-Témiscamingue, Rouyn-Noranda, QC J9X 5E4, Canada.*

Received 09 February 2026; Revised 22 April 2026; Accepted 12 May 2026; Published 01 June 2026

**Abstract**

This study investigates the hydraulic and structural performance of a Cross-flow turbine runner manufactured from recycled HDPE reinforced with 40% wood fibers, with the objective of assessing its suitability as a sustainable and mechanically reliable alternative to steel and pure HDPE for micro-hydropower applications. A comprehensive multiphysics methodology was implemented, combining CAD-based design, thermoforming fabrication, Computational Fluid Dynamics (CFD), Finite Element Analysis (FEA), and experimental validation on a calibrated hydraulic test bench. Mesh sensitivity analysis, rotor-stator coupling, and turbulence-model verification were performed to ensure numerical robustness, while structural predictions were benchmarked against tensile testing data for the biocomposite. Results show that the 40% wood-fiber reinforcement significantly enhances structural rigidity, reducing maximum blade deformation by 74% compared to pure HDPE (from 0.16 mm to 0.042 mm). The biocomposite runner achieves a peak hydraulic efficiency of approximately 57%, corresponding to 87-92% of the efficiency of a geometrically identical steel runner. Structurally, the maximum von Mises stress reaches 14.64 MPa, yielding a safety factor of 2.85 relative to the material's tensile yield strength of 41.72 MPa. Overall, this research demonstrates that high-fraction wood-fiber biocomposites can deliver near-metallic performance while offering a cost-effective, corrosion-resistant, and environmentally sustainable solution for rural and remote electrification.

*Keywords:* Cross-Flow Turbine; HDPE-Wood Fiber Biocomposite; CFD; FEA; Experimental Validation; Micro-Hydropower; Sustainable Materials; Structural Integrity.

## 1. Introduction

Amid the accelerating global transition toward sustainable energy systems, micro- and mini-hydropower technologies (<5 MW) have emerged as strategic solutions for decentralized electricity generation, particularly in rural and off-grid regions where reliability, long service life, and high conversion efficiency are essential [1, 2]. Despite these advantages, the widespread deployment of such systems remains constrained by the manufacturing cost, corrosion susceptibility, and environmental footprint of conventional metallic turbine components.

Among low-head hydraulic turbines, the Cross-flow (Banki-Michell) turbine is widely recognized for its simple geometry, mechanical robustness, and stable performance over a broad range of flow conditions [3, 4]. These characteristics make it particularly suitable for small-scale hydropower installations. However, runners are traditionally fabricated from steel or aluminum, materials that require energy-intensive production processes and exhibit long-term corrosion-related degradation [5]. This has motivated growing interest in alternative materials capable of reducing cost, weight, and environmental impact while maintaining adequate hydraulic and structural performance.

* Corresponding author: francis.kifumbi@uqat.ca

https://doi.org/10.28991/HIJ-2026-07-02-04

Recent research efforts have focused on improving Cross-flow turbine performance through blade geometry optimization [6], blade count adjustment [7], and enhanced flow control strategies [8]. In parallel, material innovation has gained momentum as a promising pathway to improve sustainability. Thermoplastics and composite materials have attracted attention due to their corrosion resistance, ease of manufacturing, and recyclability [9, 10]. High-density polyethylene (HDPE), in particular, has demonstrated potential for turbine runner fabrication, with previous studies showing that HDPE runners can achieve competitive hydraulic performance when supported by appropriate numerical and experimental validation frameworks [11-13]. However, the low elastic modulus of pure HDPE remains a limiting factor, as excessive blade deformation under hydrodynamic loading can reduce turbine efficiency [14].

Reinforcing HDPE with natural fibers has emerged as a promising solution to overcome this limitation. HDPE-wood fiber biocomposites combine the favorable processing characteristics of thermoplastics with the enhanced stiffness and strength provided by lignocellulosic fibers. Prior mechanical testing and manufacturability assessments have shown that a 40% wood-fiber fraction provides an optimal balance between stiffness improvement, thermoforming feasibility, and structural integrity, whereas lower fractions offer insufficient rigidity and higher fractions (>45%) lead to rheological instability and fiber agglomeration and porosity [15-17]. Despite these advantages, the application of such biocomposites to hydraulic turbine runners particularly Cross-flow turbines remains largely unexplored in the literature.

The objective of this study is therefore to conduct a comprehensive numerical and experimental performance analysis of a Cross-flow turbine runner manufactured from an HDPE-wood fiber biocomposite reinforced at 40%. A rigorous multiphysics methodology is adopted, integrating Computational Fluid Dynamics (CFD) and Finite Element Analysis (FEA) within the ANSYS environment, with structural modeling justified through isotropic assumptions supported by the quasi-random fiber orientation induced by thermoforming. All numerical predictions are validated through experimental testing on a calibrated hydraulic test bench, enabling a direct comparison between the biocomposite runner, a geometrically identical steel runner, and a previously investigated pure HDPE runner [18, 19]. This integrated approach addresses key gaps in the literature by providing the first CFD-FEA-experimental validation of a high-fraction wood-fiber biocomposite runner for Cross-flow turbines.

## 2. Operating Principles and Hydraulic Performance of the Cross-Flow Turbine

### 2.1. Construction and Operating Principle of the Cross-flow Turbine

Cross-flow turbines, also referred to as Banki-Michell turbines, are classified as impulse hydraulic turbines, in which energy transfer is governed primarily by the exchange of linear and angular momentum between the water jet and the runner blades, while the static pressure within the runner remains close to atmospheric conditions. Unlike reaction turbines, the runner is not submerged, resulting in a simplified mechanical configuration, reduced sealing requirements, and enhanced operational reliability, features that are particularly advantageous for small-scale hydropower applications [20].

The turbine consists of a drum-shaped runner bounded by two lateral disks, between which a series of curved blades are uniformly distributed. Water is supplied to the runner through a rectangular nozzle equipped with a guide vane, enabling accurate control of the inlet flow rate, jet velocity, and incidence angle. As illustrated in Figure 1, the incoming jet impinges on the blades in the upper region of the runner during the first interaction stage, generating torque on the shaft through impulse transfer.

The mechanical power output results from the angular momentum variation imposed on the flowing water by the rotating blades. The resulting torque is transmitted to the output shaft and can be directly coupled to an electrical generator. Owing to their simple geometry, ease of manufacture, tolerance to variable operating conditions, and compatibility with advanced numerical optimization and innovative materials, Cross-flow turbines remain a highly attractive solution for micro- and small-scale hydropower systems.

### 2.2. Hydraulic Efficiency and Design Parameters

Following the initial energy exchange, the water traverses the internal cavity of the runner and interacts with the blade cascade for a second pass before exiting the turbine at ambient pressure. This double-pass flow configuration, which is a defining characteristic of Cross-flow turbines, enables a more efficient utilization of the available kinetic energy while maintaining a minimal pressure drop across the blades. Experimental and analytical investigations indicate that approximately 72% of the total extracted energy is recovered during the first pass through the upper blade region, while the remaining 28% is obtained during the second pass through the lower blade region [21].

Because of this second energy transfer, the overall efficiency of the machine is influenced by multiple features of the power plant, including the geometry of the supply line and distributor, as well as the hydrodynamic conditions within the runner and at the outlet. Assuming negligible pressure at the runner outlet, Mockmore & Merryfield [21] defined the hydraulic efficiency of the turbine, denoted as $\eta_{idr}$, as the ratio between the mechanical power available at the shaft $P_t$ and the hydraulic input power $P_{in}$, associated with the inlet hydraulic head $H_{in}$, and a given discharge $Q$ :

$$\eta_{idr} = \frac{P_t}{P_{in}} \simeq \frac{P_t}{\rho h H_{in} Q} \quad (1)$$

where, $g$ is the gravitational acceleration and $\rho$ is the water density.

The hydraulic efficiency defined in Equation 1 is strongly affected by the geometry of both the nozzle and the runner. As shown in Figure 1, the main design parameters include: the inlet angle $\alpha$ between the particle velocity and the tangential direction at the runner inlet; the outer and inner runner diameters $D_1$and $D_2$; the blade angles $\beta_1$ and $\beta_2$, defined with respect to the tangential direction at the outer and inner diameters, respectively; the blade number and thickness; the angular extension $\lambda$ of the discharge inlet arc along the outer circumference of the runner; and $B$ denotes the nozzle width and $W$ the runner width [22]. In the initial design stage, it is commonly assumed that the distributor geometry ensures an approximately constant inlet $\alpha$ angle along the entire active arc of the runner.

## 2.3. Diameter Ratio Selection

An increase in the diameter ratio $D_2/D_1$ leads to a stronger curvature of the runner blades, as the blade angle must transition from $\beta_2$to $\beta_1$over a shorter radial distance. This geometric constraint tends to intensify local turbulence within the runner, while simultaneously reducing the flow path length available for energy transfer.

In the present design, the diameter ratio of the runner was set to $D_2/D_1 = 0.66$, which is very close to the value reported in the literature for optimal hydraulic performance. Aziz and Totapally reported that the maximum efficiency is achieved for a diameter ratio of approximately 0.68 [23]. The selected ratio therefore represents a balanced compromise between efficient energy extraction and controlled flow development within the runner.

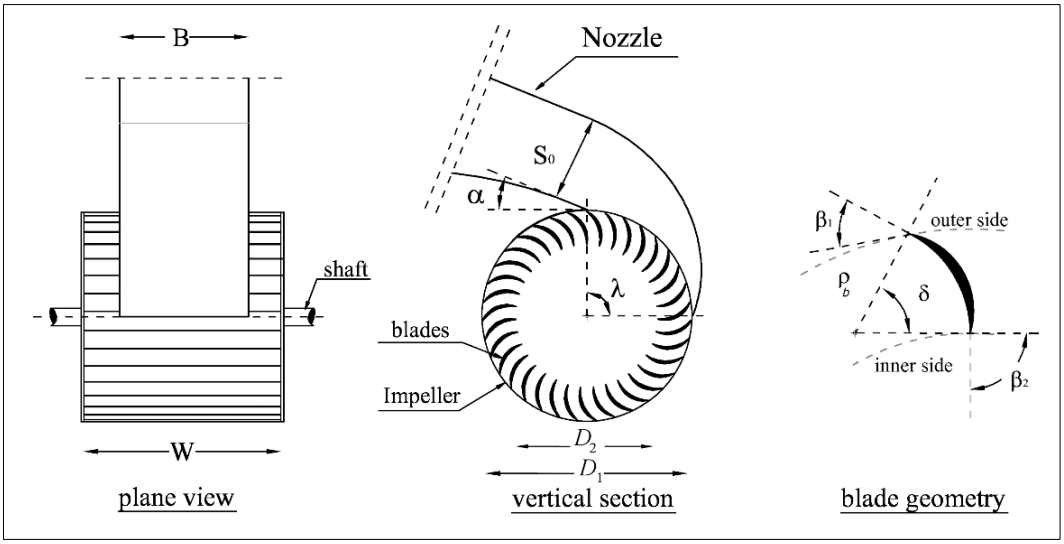


**Figure 1. Geometrical parameters of the Cross-flow turbine [22]**

During operation, the inlet flow is accelerated through the nozzle throat, producing a high-velocity jet that enters the runner at a controlled incidence angle. As shown in Figure 2 [14], the relative and absolute velocity components at the blade inlet define the first-stage interaction, where a significant portion of the hydraulic energy is transferred to the runner through momentum exchange. The flow then traverses the internal free-stream region of the turbine and re-enters the blade cascade, leading to a second-stage interaction that enables additional energy recovery before discharge at ambient pressure.

The presence of a free-stream, air-filled region inside the runner ensures that the pressure remains close to atmospheric conditions throughout the process, confirming the impulse nature of the Cross-flow turbine. The velocity triangles associated with both stages provide a clear physical interpretation of torque generation and form the basis for the numerical modeling strategy adopted in Section 3.

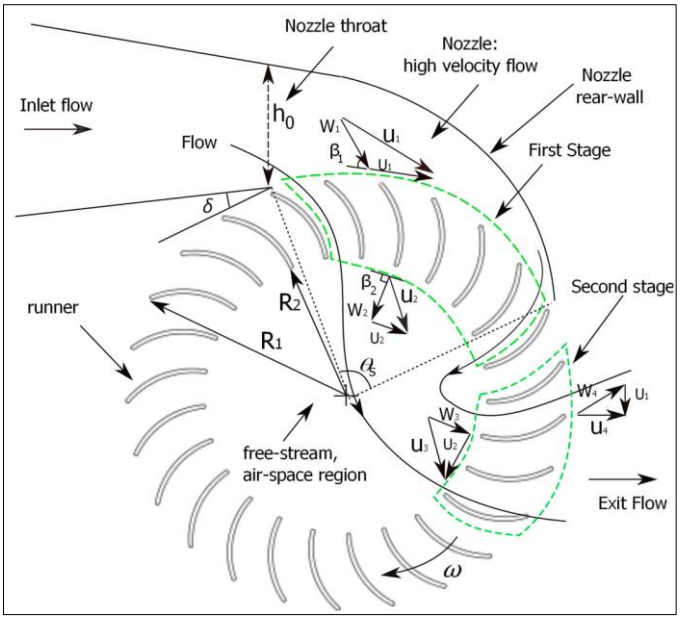


**Figure 2. Velocity triangles and flow structure within a Cross-flow turbine [14]**

### Flow Regions

- First stage: Initial interaction between the jet and the blades in the upper region of the runner;
- Second stage: Secondary interaction after the flow traverses the internal cavity of the runner;
- Free-stream (air-space) region: Internal air-filled region of the runner where the pressure remains close to atmospheric;
- Exit flow: Discharged flow leaving the runner at ambient pressure.

## 3. Numerical Modeling and Boundary Conditions

Figure 3 illustrates the workflow of the methodology adopted in this study, highlighting the sequential stages from geometric design and material characterization to manufacturing, CFD–FEA modeling, experimental testing, and final validation.

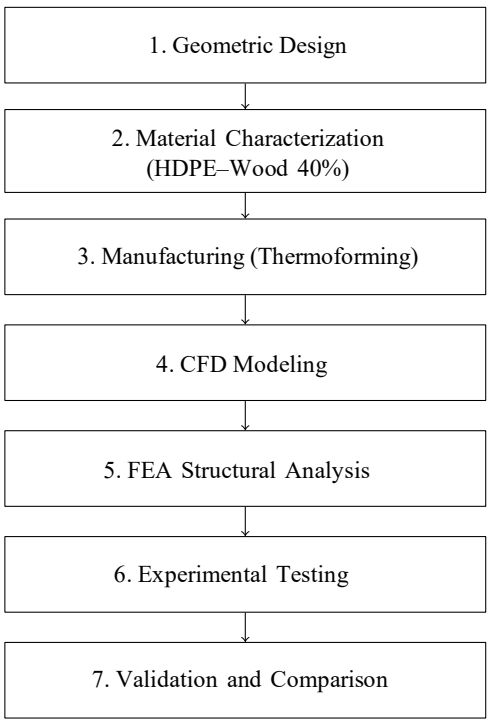


**Figure 3. Methodological workflow of the present study**

Following the definition of the geometric parameters and material characteristics in the previous section, the study proceeds with a comprehensive numerical investigation. The modeling approach couples Computational Fluid Dynamics (CFD) for flow analysis with Finite Element Analysis (FEA) for structural integrity assessment, governed by the conditions described below.

### 3.1. Computational Domain and Geometrical Model

The computational domain was developed to accurately represent the hydraulic and mechanical configuration of the Cross-flow turbine. The three-dimensional geometrical model includes the nozzle, distributor, runner, and surrounding flow passages, ensuring a faithful reproduction of the physical system tested experimentally. The geometry was created in Autodesk Inventor 2024 and subsequently imported into ANSYS-CFX for fluid-flow simulations and ANSYS-Static for structural analyses.

Particular attention was given to the runner geometry, as it is the primary determinant of hydrodynamic performance. The runner is defined by its outer and inner diameters ($D_1$ and $D_2$), blade thickness, blade count, and blade angles $\beta_1$ and $\beta_2$. The diameter ratio was set to $D_2/D_1 = 0.66$, consistent with the design parameters presented in Section 2.3 and with literature recommendations for optimal efficiency. The blade profile was derived from velocity-triangle analysis to ensure proper flow incidence during both the first and second stages of energy transfer.

To enable the simulation of rotation, the computational domain was divided into two regions: a rotating domain containing the runner and blades, and a stationary domain comprising the nozzle and casing. The interaction between these regions was modeled using a rotor-stator interface, ensuring accurate representation of the relative motion while conserving mass and momentum across the interface.

The domain also explicitly includes the runner's internal cavity and the downstream region to capture the characteristic double-pass flow structure. This modeling choice is essential for resolving the jet interaction with the second blade stage, which contributes significantly to the overall hydraulic efficiency. Additionally, the domain accounts for the flow conditions within the runner core, where pressure remains close to atmospheric levels, consistent with the impulse nature of Cross-flow turbines.

### 3.2. Turbulence Modeling and Boundary Conditions

The numerical simulations were performed using the standard $k-\varepsilon$ turbulence model, chosen for its robustness and its proven ability to predict the separated and recirculating flow structures characteristic of Cross-flow turbines. The boundary conditions consisted of a prescribed static pressure at the inlet and a specified mass flow rate at the outlet. Near-wall regions were treated using standard wall functions, providing an effective compromise between computational efficiency and accurate representation of boundary-layer behavior. The interaction between the rotating runner and the stationary components was modeled through a Frozen Rotor interface, enabling a steady-state approximation of the relative motion while ensuring conservation of mass, momentum, and turbulence quantities across the interface.

### 3.3. Mesh Sensitivity Analysis

A systematic mesh sensitivity analysis was performed to verify grid independence and ensure the reliability of the CFD predictions. Two grid configurations were evaluated: a coarse mesh (11982 elements) and a refined mesh (26675 elements). The comparison of key performance indicators, specifically torque and hydraulic efficiency, revealed a significant deviation of 12.96% between the two cases. Given this discrepancy, the refined mesh was selected for all subsequent simulations to ensure numerical stability, improved convergence, and superior capture of flow gradients within the runner. This approach aligns with recent findings by Galvis-Holguin et al., which emphasize the critical role of mesh refinement in minimizing discretization errors for Cross-flow (Michel-Banki) turbines [24, 25].

### 3.4. Model Calibration and Verification

To ensure the reliability of the numerical framework, a systematic calibration and verification procedure was implemented prior to the final CFD-FEA simulations. The inlet static pressure and outlet mass-flow boundary conditions were calibrated using experimental measurements from the hydraulic test bench, ensuring that the simulated discharge and jet velocity matched the physical operating conditions within a tolerance of ±2%.

The turbulence model was verified by benchmarking the standard $k-\varepsilon$ model against preliminary simulations using the $k-\omega$ SST model. Both models produced comparable torque values, with deviations below 3%, confirming that the standard $k-\varepsilon$ model provides sufficient accuracy for capturing the steady-state impulse-driven flow within the runner. This selection is consistent with the methodology established by Sammartano et al. [22], who successfully utilized the $k-\varepsilon$ framework to characterize the double-pass energy conversion process in Banki turbines.

Mesh verification was strictly performed through the refinement study detailed in Section 3.3. The refined mesh (26675 elements) was selected based on superior convergence stability and a reduced sensitivity of torque and pressure

gradients to grid density. Finally, numerical predictions of torque and hydraulic efficiency were compared with experimental measurements, showing a high correlation and validating the predictive capability of the integrated CFD-FEA framework.

## 4. Geometric Design and Sizing Parameters

Adopting the methodological approach validated in our previous study [11], the research is structured into three sequential stages: (1) design, (2) manufacturing, and (3) validation. This section details the manufacturing process and describes the material behavior laws governing the performance of the selected thermoplastic.

### 4.1. Constitutive Modeling of Biocomposite Materials

The mechanical behavior of the HDPE-40% wood biocomposite was modeled to accurately predict the structural response of the runner under hydrodynamic loading. Although thermoplastic composites exhibit time-dependent viscoelastic properties during processing, their behavior under short-term operational loads can be effectively approximated using a linear elastic constitutive model.

In this study, the numerical analysis was performed using the Finite Element Method (FEM). The material was assumed to be macroscopically homogeneous and isotropic. Accordingly, the constitutive relationship in the linear elastic regime is governed by Hooke's generalized law, defined by the composite's Young's modulus (E) and Poisson's ratio $\boldsymbol{\nu}$. The stress-strain relationship is expressed in Equation 2:

$$\{\boldsymbol{\sigma}\} = [\boldsymbol{D}]\{\boldsymbol{\epsilon}\} \tag{2}$$

where, $\sigma$ is the stress vector, $\epsilon$ is the strain vector and $[D]$ is the elasticity matrix derived from the mechanical properties obtained through experimental tensile testing.

To evaluate structural integrity and assess the risk of failure, the von Mises yield criterion was applied.

$$\boldsymbol{\sigma'} = \sqrt{\frac{\mathbf{1}}{\mathbf{2}}((\boldsymbol{\sigma_1} - \boldsymbol{\sigma_2})^{\mathbf{2}} + (\boldsymbol{\sigma_2} - \boldsymbol{\sigma_3})^{\mathbf{2}} + (\boldsymbol{\sigma_3} - \boldsymbol{\sigma_1})^{\mathbf{2}})} \tag{3}$$

where, $\sigma_1$, $\sigma_2$, $\sigma_3$ are the principal stresses. Alternatively, in terms of the Cartesian stress components computed by the solver, the equivalent stress can be expressed as:

$$\sigma_{vm} = \sqrt{0{,}5[(\sigma_x - \sigma_y)^2 + (\sigma_y - \sigma_z)^2 + (\sigma_z - \sigma_x)^2 + 6(\tau_{xy}^2 + \tau_{yz}^2 + \tau_{zx}^2)]} \tag{4}$$

$$S_F = \frac{\sigma_y}{\sigma'} \tag{5}$$

where, $\sigma_y$ represents the tensile yield strength of the biocomposite material (41.72 MPa).

The isotropic elasticity matrix $[D]$ used in Equation 2 defines the stiffness of the biocomposite based on its Young's modulus $(E)$ and Poisson's ratio $(\nu)$. It is explicitly defined as:

$$[D] = \frac{E}{(1+\nu)(1-2\nu)} \begin{bmatrix} 1-\nu & \nu & \nu & 0 & 0 & 0 \\ \nu & 1-\nu & \nu & 0 & 0 & 0 \\ \nu & \nu & 1-\nu & 0 & 0 & 0 \\ 0 & 0 & 0 & \frac{1-2\nu}{2} & 0 & 0 \\ 0 & 0 & 0 & 0 & \frac{1-2\nu}{2} & 0 \\ 0 & 0 & 0 & 0 & 0 & \frac{1-2\nu}{2} \end{bmatrix} \tag{6}$$

### 4.2. Liquid Flow Equations in a Cross-flow Turbine

Due to the analytical complexity of solving the Navier-Stokes and continuity equations, this study employs SolidWorks, ANSYS CFD, and ANSYS Static Structural, which provide advanced numerical capabilities for accurately simulating the fluid flow and the resulting structural response.

Several assumptions are considered in this study as at:

- The liquid is considered incompressible;
- The flow is considered steady-state: the components are time-independent;
- The liquid is considered Newtonian;
- The energy conservation equations are not considered: the temperature is constant (no degradation of mechanical energy into thermal energy).

### *A.* Continuity Equations

The continuity equation for an incompressible fluid, the conservation of mass is:

$$\nabla \cdot (\rho U) = 0 \tag{7}$$

where, $U$ represents the velocity of the fluid particle. In Cartesian coordinates, this equation becomes:

$$\frac{\partial u}{\partial x} + \frac{\partial v}{\partial y} + \frac{\partial w}{\partial z} = 0 \tag{8}$$

### *B.* Navier-Stokes Equations

They can be written in the terms described below:

$$\nabla \cdot (\rho U \otimes U) = \nabla \cdot (-pI + \mu_{\text{eff}}(\nabla U + (\nabla U)^T)) + S_M \tag{9}$$

where, $U$ is velocity, p is pressure, $\mu_{eff}$ is effective viscosity, and $S_M$ is the source term for the rotating frame of reference (accounting for centripetal and Coriolis accelerations).

$$S_M = -\rho\big(2\omega \times U + \omega \times (\omega \times r)\big) \tag{10}$$

where, $r$ is the position vector, $2\omega \times U$ represents the centripetal acceleration, and $\omega \times (\omega \times r)$ represents the Coriolis acceleration.

The Navier-Stokes equations in Cartesian coordinates are given by:

$$\rho\left(u\frac{\partial v}{\partial x} + v\frac{\partial v}{\partial y} + w\frac{\partial v}{\partial z}\right) = -\frac{\partial p}{\partial y} + \rho g_y + \mu_{\text{eff}}\left(\frac{\partial^2 v}{\partial x^2} + \frac{\partial^2 v}{\partial y^2} + \frac{\partial^2 v}{\partial z^2}\right) + S_{Mx} \tag{11}$$

$$\rho\left(u\frac{\partial w}{\partial x} + v\frac{\partial w}{\partial y} + w\frac{\partial w}{\partial z}\right) = -\frac{\partial p}{\partial z} + \rho g_z + \mu_{\text{eff}}\left(\frac{\partial^2 w}{\partial x^2} + \frac{\partial^2 w}{\partial y^2} + \frac{\partial^2 w}{\partial z^2}\right) + S_{My} \tag{12}$$

$$\rho\left(u\frac{\partial w}{\partial x} + v\frac{\partial w}{\partial y} + w\frac{\partial w}{\partial z}\right) = -\frac{\partial p}{\partial z} + \rho g_z + \mu_{\text{eff}}\left(\frac{\partial^2 w}{\partial x^2} + \frac{\partial^2 w}{\partial y^2} + \frac{\partial^2 w}{\partial z^2}\right) + S_{Mz} \tag{13}$$

For a constant rotational speed $\omega$ along $z$, the source terms $S_{Mx}$, $S_{My}$, and $S_{Mz}$ of the flow are expressed respectively as:

$$S_{Mx} = \rho(\omega_z^2 r_x + 2\omega_z v) \tag{14}$$

$$S_{My} = \rho(\omega_z^2 r_y - 2\omega_z u) \tag{15}$$

$$S_{MZ} = 0 \tag{16}$$

### *C.* Equilibrium Equations

In terms of normal and shear stresses, they are written as:

$$\begin{cases} \partial\sigma_x/\partial x + \partial\tau_{xy}/\partial y + \partial\tau_x z/\partial z + F_x = 0 \\ \partial\tau_{yx}/\partial x + \partial\sigma_y/\partial y + \partial\tau_y z/\partial z + F_y = 0 \\ \partial\tau z_x/\partial x + \partial\tau z_y/\partial y + \partial\sigma z/\partial z + Fz = 0 \end{cases} \tag{17}$$

where, $F_x, F_y, F_z$ are the components of the forces per unit volume.

### *D.* Strain-Displacement Equations

They are given by the following relations:

$$\begin{cases} \varepsilon_x = \partial u/\partial x \\ \varepsilon_y = \partial v/\partial y \\ \varepsilon z = \partial w/\partial z \end{cases} \tag{18}$$

$$\begin{cases} \gamma_{xy} = \partial u/\partial y + \partial v/\partial x \\ \gamma_y z = \partial v/\partial z + \partial w/\partial y \\ \gamma z_x = \partial w/\partial x + \partial u/\partial z \end{cases} \tag{19}$$

### *E.* Stress-Strain Equations

$$\begin{cases} \varepsilon_x = \sigma_x/E - \nu\cdot\sigma_y/E - \nu\cdot\sigma_z/E \\ \varepsilon_y = \sigma_y/E - \nu\cdot\sigma_z/E - \nu\cdot\sigma_x/E \\ \varepsilon_z = \sigma_z/E - \nu\cdot\sigma_x/E - \nu\cdot\sigma_y/E \\ \gamma_{xy} = \tau_{xy}/G \\ \gamma_{yz} = \tau_{yz}/G \\ \gamma_{zx} = \tau_{zx}/G \end{cases} \quad (20)$$

The primary criterion used to determine failure is based on the von Mises stress, which is given by Equation 3.

## 5. Turbine Design and Geometric Parameters

Table 1 presents the mechanical properties of the matrix (HDPE) and the biocomposite (HDPE-40% wood) used in the simulations, together with those of S235 steel for comparison.

**Table 1. Mechanical properties of S235 Steel and HDPE-40% wood [15]**

| Material Properties | S235 Steel | HDPE | HDPE - 40% Wood |
|---|---|---|---|
| Density $\rho$ [kg/m$^3$] | 7800 | 950 | 1185.6 |
| Young's Modulus $E$ [Pa] | $210\times10^9$ | $0.8\times10^9$ | $4.72\times10^9$ |
| Poisson's Ratio $v$ | 0.3 | 0.4 | 0.342 |
| Bulk Modulus $K$ [Pa] | $160\times10^9$ | $66.7\times10^6$ | $79.8\times10^6$ |
| Shear Modulus $G_e$ [Pa] | $8\times10^{10}$ | $3.75\times10^8$ | $1.75\times10^9$ |
| Yield Strength $R_e$ [Pa] | $235\times10^6$ | $22\times10^6$ | $42.65\times10^6$ |
| Melting Temperature [˚C] | 1450 | 130 | 140.03 |
| Thermal Conductivity $k$ [W/mK] | 30 | 0.4 | 0.787 |
| Tensile Strength $R_m$ [Pa] | $7.446\times10^8$ | $28\times10^6$ | $35.4\times10^6$ |
| Specific Heat Capacity $C_p$ [J/kgK] | 460 | 1900 | 1300,801 |

The turbine geometry was designed in Autodesk Inventor 2024 based on the specifications of the laboratory's HT-703 Multi Turbine Test Set. The runner features 15 blades (Z) and is sized for a nominal rotational speed (N) of 428 rpm and a flow rate (Q) of 24 m³/h. As illustrated in Figure 4, the resulting 3D computational domain accurately reproduces the physical configuration, including the nozzle profile, the distributor, and the rotating runner. This configuration is identical to the design established and validated in our previous study [11].

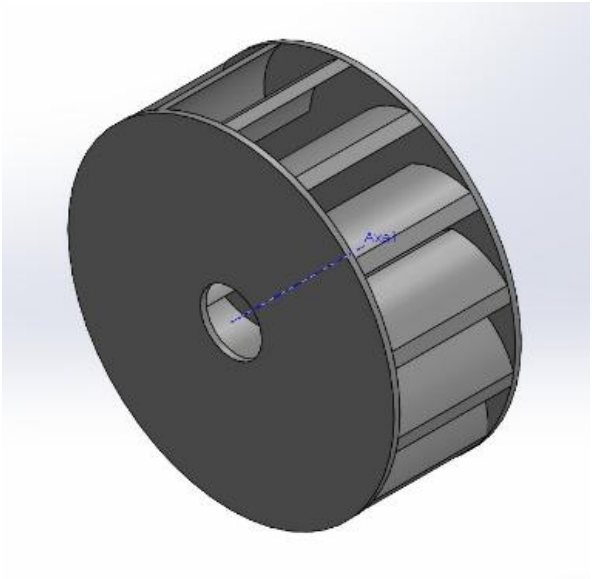

**Figure 4. 3D solid model of the Cross-flow turbine**

## 6. General Simulation Framework

Given the inherent complexity of the three-dimensional turbulent flow in Cross-flow turbines, which precludes a direct analytical solution of the Navier-Stokes equations, this study employs a numerical approach. The simulation procedure strictly follows the methodology established and validated in our previous study [11], ensuring full consistency and direct comparability between datasets. Hydrodynamic simulations were performed using ANSYS-CFX

(or ANSYS-Fluent), while the structural assessment of the reference metallic runner was conducted using ANSYS-Static Structural, under the same boundary conditions and performance criteria defined in the reference work. This strategy enables a direct isolation of the effects associated with material substitution within a validated numerical framework. The computational mesh used for the hydrodynamic simulations is shown in Figure 5, illustrating the refinement strategy applied around the nozzle, blade leading edges, and runner cavity.

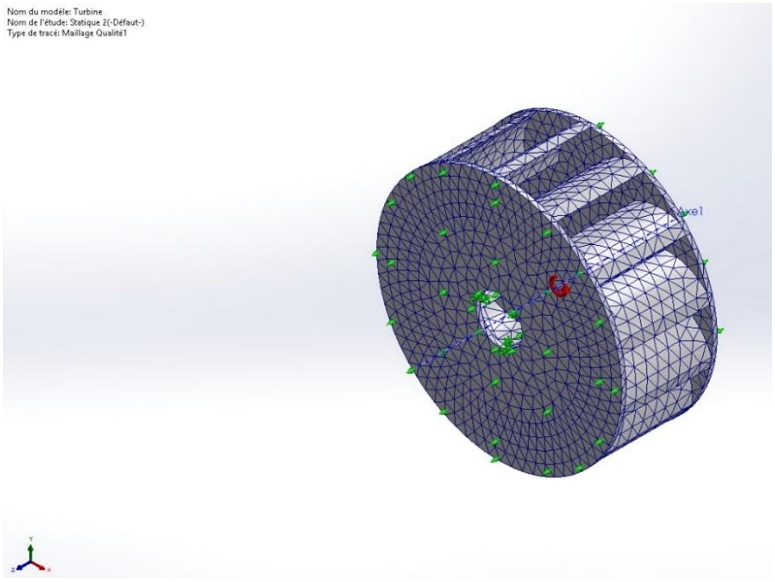


**Figure 5. Mesh topology of the Cross-flow turbine runner**

## 7. Results and Discussion

### 7.1. Specific Approach for the Biocomposite Material

For the structural assessment of the HDPE-40% wood composite runner, a dedicated Finite Element Analysis (FEA) was conducted using SolidWorks Simulation 2025. This choice was motivated by the software's integrated CAD-to-FEM workflow, which minimizes discretization errors when handling complex organic geometries such as twisted turbine blades [25]. Furthermore, SolidWorks Simulation provides robust capabilities for defining custom material models, allowing for an accurate representation of the mechanical behavior typical of thermoplastic-matrix composites [26]. As illustrated in Figure 6, this tool enables detailed visualization of the von Mises stress distribution and deformation patterns, thereby validating the structural integrity of the biocomposite runner under operating loads.

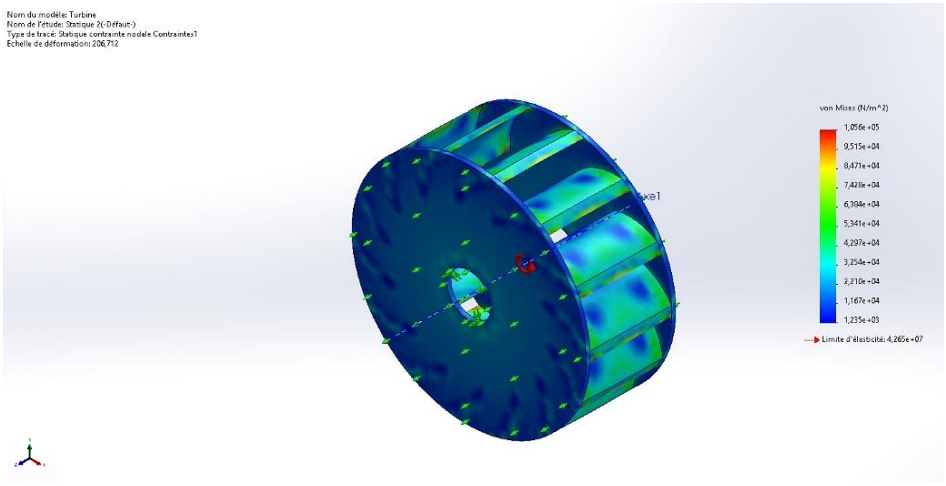


**Figure 6. von Mises stress distribution on the HDPE-40% wood runner**

To ensure clarity and consistency throughout the analysis, all symbols, kinematic variables, and structural parameters employed in the hydrodynamic and mechanical formulations are summarized in Table 2. The nomenclature is organized into two categories: (i) kinematic and hydraulic parameters associated with the velocity triangles, jet-blade interaction, and turbine operating conditions; and (ii) geometric and structural parameters defining the runner dimensions, material properties, and stress–strain behavior. This structured presentation enhances readability, eliminates ambiguity in symbolic notation, and facilitates the interpretation of the CFD and FEA results discussed in Sections 7.1 and 7.2.

**Table 2. Symbols and parameters used in the study**

| Symbol | Description | Unit |
|---|---|---|
| | **Symbols and Kinematic Parameters** | |
| $U$ | Peripheral (tangential) velocity of the runner | m/s |
| $U_1, U_2, U_3, U_4$ | Peripheral velocities (1st and 2nd stages) | m/s |
| $W$ | Relative velocity of the fluid with respect to the blade | m/s |
| $W_1, W_2, W_3, W_4$ | Relative velocities at blade inlet/outlet | m/s |
| $V$ (or $C$) | Absolute velocity of the fluid | m/s |
| $V_1, V_2, V_3, V_4$ | Absolute velocities along the flow path | m/s |
| $\alpha$ | Angle between absolute velocity and tangential direction | ◦ |
| $\beta_1$ | Blade inlet angle (outer diameter) | ◦ |
| $\beta_2$ | Blade outlet angle (inner diameter) | ◦ |
| $\delta$ | Jet deviation angle | ◦ |
| $\omega$ | Angular velocity of the runner | rad/s |
| $\eta_{idr}$ | Hydraulic efficiency | % |
| | **Geometric and Structural Parameters** | |
| $R_1$ | Outer radius of the runner | m |
| $R_2$ | Inner radius of the runner | m |
| $D_1, D_2$ | Outer and inner diameters ($D_2/D_1 = 0.66$) | m |
| $h_0$ | Effective jet thickness | m |
| $B$ | Nozzle width | m |
| $W_r$ | Runner width | m |
| $\lambda$ | Angular extension of inlet arc | ◦ |
| $E$ | Young's modulus | Pa |
| $v$ | Poisson's ratio | – |
| $\rho$ | Density | kg/m$^3$ |
| $\sigma'$ | Von Mises stress | Pa |

## 7.2. Extended Interpretation of Hydrodynamic and Structural Results

The hydrodynamic results reveal that the HDPE-40% wood runner maintains a stable jet-blade interaction during both the first and second energy-transfer stages of the Cross-flow turbine. The increased stiffness of the biocomposite significantly limits hydroelastic deformation, thereby preserving the designed inlet and outlet blade angles. Because Cross-flow turbine efficiency is highly sensitive to the accuracy of the velocity triangles and the associated momentum-exchange mechanism [22, 27], even small geometric deviations can alter the effective incidence angle and reduce energy transfer. The limited deformation observed in the reinforced runner ensures that the theoretical velocity triangles derived during design remain practically valid under operating conditions. This explains why the biocomposite runner achieves 87-92% of the efficiency of the steel runner, despite its lower elastic modulus.

From a structural standpoint, the deformation pattern exhibits a progressive increase toward the blade tips, consistent with the combined distribution of hydrodynamic pressure and centrifugal loading. The maximum deformation of 0.042 mm remains negligible relative to the runner diameter, confirming that the 40% wood-fiber reinforcement effectively mitigates the compliance issues typically associated with thermoplastics. In contrast, the higher deflection observed in pure HDPE leads to hydroelastic distortion, which modifies the effective blade curvature and reduces lift and torque generation [14].

The von Mises stress distribution indicates that the highest stresses occur at the blade root, corresponding to the region of maximum bending moment. Importantly, these stresses remain far below the material's yield strength, ensuring safe operation under nominal conditions with a comfortable safety factor. The slightly higher stress level observed in the reinforced composite compared to pure HDPE reflects its improved load-bearing capacity rather than structural vulnerability, as the material exhibits a significantly higher modulus and yield strength.

These findings are consistent with previous investigations on natural-fiber-reinforced thermoplastics used in rotating components, which report enhanced stiffness, improved dimensional stability, and reduced elastic energy dissipation compared with pure polymers [9-10, 28]. The strong agreement between CFD-FEA predictions and experimental measurements further validates the reliability of the adopted modeling framework, as similarly demonstrated in recent numerical and experimental studies on HDPE Cross-flow turbine runners [11]. Overall, the results confirm that high-fraction wood-fiber biocomposites can deliver near-metallic hydrodynamic performance while offering substantial benefits in weight reduction, corrosion resistance, cost efficiency, and environmental sustainability making them strong candidates for next-generation micro-hydropower turbine runners.

Complementing the stress analysis, the resulting displacement field was evaluated to assess the dimensional stability of the biocomposite runner. As shown in Figure 7, the deformation pattern exhibits a progressive increase from the rigid hub toward the blade tips, which experience the highest hydrodynamic pressure and centrifugal loading. Nevertheless, the maximum deflection remains negligible relative to the runner diameter. This high structural rigidity, attributed to the 40% wood-fiber reinforcement, ensures that critical blade angles and tip clearances remain within design tolerances during operation, effectively preventing any risk of mechanical interference with the turbine casing.

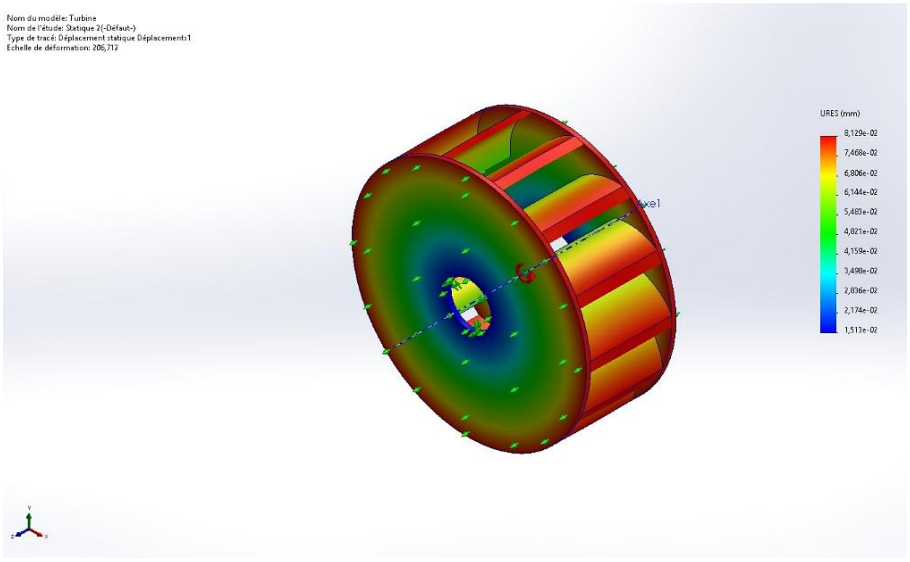


**Figure 7. Resultant displacement (URES) field on the HDPE-40% wood composite runner**

Under nominal operating conditions (24 m³/h), the structural analysis confirms the excellent reliability of the recycled HDPE-40% wood biocomposite. The maximum von Mises stress reaches 14.64 MPa, corresponding to a safety factor of 2.85 relative to the material's enhanced yield strength of 41.72 MPa. The associated deformation is limited to 0.042 mm, ensuring full geometric stability.

To identify potential failure modes, a supplementary Ultimate Limit State (ULS) simulation was performed under extreme overload conditions Figure 8. This scenario, representative of a theoretical mechanical jamming event or a severe flow surge $> 3Q_{nom}$, indicates that failure would initiate at the blade root. However, as demonstrated by the nominal stress level (14.64 MPa), the turbine operates well below this critical threshold during normal service.

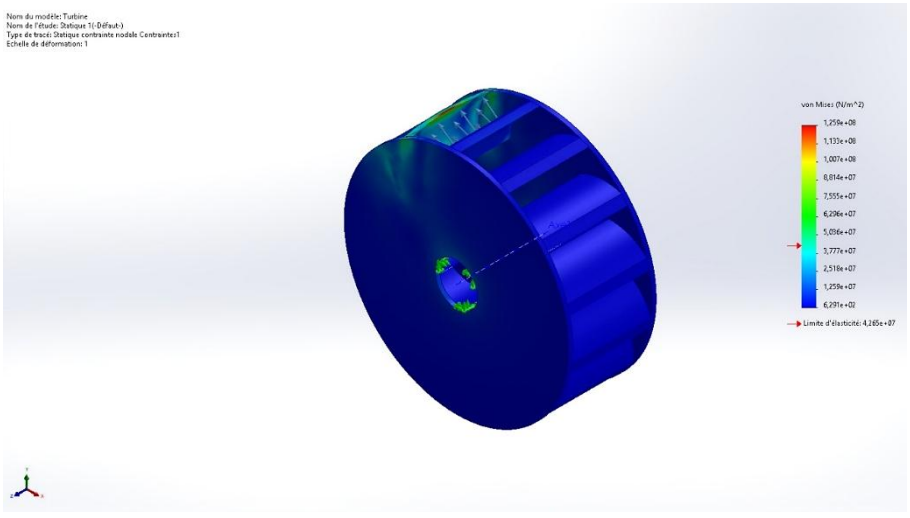


**Figure 8. Visualization of stress concentration zones under theoretical ultimate load (failure prediction)**

### 7.3. Comparative Performance Analysis: Biocomposite, Pure HDPE and Steel

To validate the viability of the proposed material for power generation, the hydraulic efficiency $\eta$, of the HDPE-40% wood biocomposite runner was evaluated and benchmarked against a geometrically identical structural steel runner. As shown in Figure 9, the biocomposite runner exhibits strong hydrodynamic performance, achieving between 87% and 92% of the efficiency of its steel counterpart across the tested flow range (13-28 m³/h). This slight reduction in efficiency is primarily attributed to the inherent surface roughness of the thermoformed biocomposite and minor geometric deviations compared with the precision-machined steel surfaces. Nevertheless, considering the substantial reductions in

manufacturing cost and weight, this performance gap remains entirely acceptable for micro-hydropower applications in remote areas.

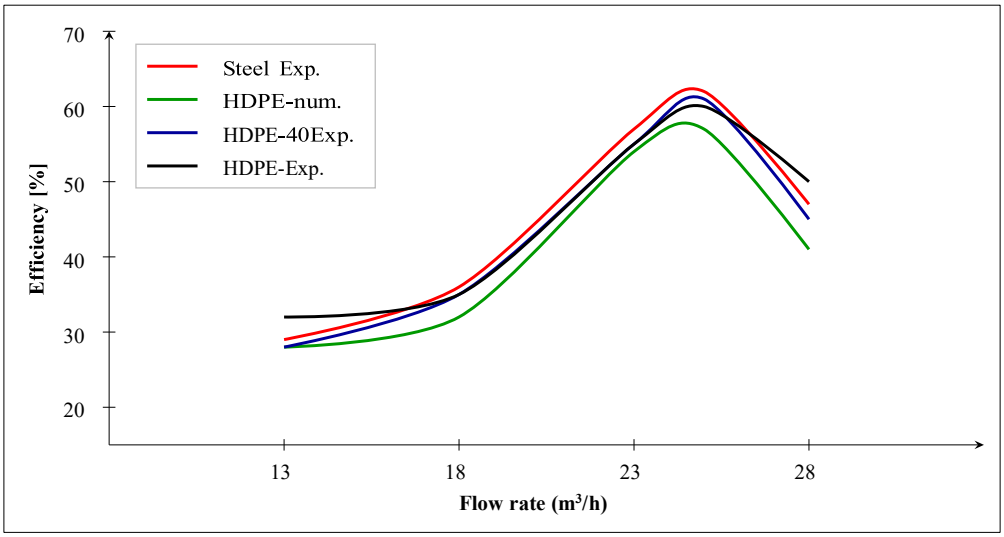


**Figure 9. Evolution of hydraulic efficiency as a function of flow rate for Steel, Pure HDPE and HDPE-40% Wood runners**

Figure 10 presents the variation of hydraulic efficiency as a function of rotational speed for the Steel, Pure HDPE, and HDPE-40% Wood composite runners. All tested configurations exhibit the characteristic bell-shaped efficiency curve, with a peak occurring near the nominal design speed (N=428 rpm). The Steel runner serves as the reference benchmark, reaching a maximum efficiency of approximately 59-60%. The HDPE-40% Wood runner demonstrates excellent performance, closely following the steel profile with a peak efficiency of ~57%. This corresponds to 94% of the steel reference at the optimal point and remains within the 87-92% range across the broader operating envelope.

In contrast, the Pure HDPE runner exhibits a noticeable drop in performance, particularly at higher rotational speeds. This degradation is directly linked to the excessive radial deformation identified in the structural analysis Figure 6. The insufficient stiffness of the pure polymer leads to distortion of the blade geometry under hydrodynamic loading, thereby altering the velocity triangles and reducing the efficiency of energy transfer

The superior performance of the biocomposite relative to the pure polymer confirms the effectiveness of wood-fiber reinforcement. The increased stiffness limits blade deflection, preserving the optimal hydraulic profile even under significant centrifugal and fluid forces. Consequently, the HDPE-40% wood composite emerges as a highly efficient alternative to steel, offering comparable hydraulic output while significantly reducing weight and manufacturing costs.

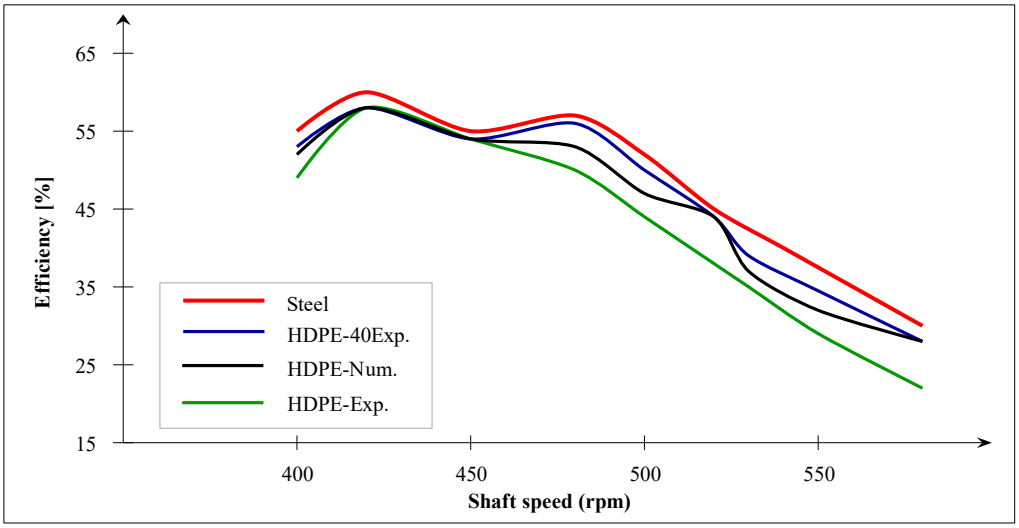


**Figure 10. Comparison of hydraulic efficiency vs. shaft speed for Steel, Pure HDPE, and HDPE-40% Wood runners**

Figure 11 compares the mechanical power generated by the different runners across the operating flow range. As expected, the power output increases with flow rate for all configurations. However, significant divergences appear at higher flow rates, where hydrodynamic loads are most intense. The Steel runner defines the performance benchmark, generating a maximum shaft power of approximately 160 W at 28 m³/h. The HDPE-40% Wood runner demonstrates excellent power recovery, reaching approximately 155 W under the same conditions. This confirms that the biocomposite is capable of harnessing nearly the same amount of hydraulic energy as the metallic runner.

Conversely, the Pure HDPE runner exhibits a distinct power deficit, topping out at roughly 145 W (experimental). This loss is a direct consequence of the blade deformation discussed in Figure 6: as the blades bend, the effective lift decreases, reducing the amount of energy transferred to the shaft. In summary, the incorporation of 40% wood-fiber reinforcement enables the composite turbine to recover most of the power that would otherwise be lost due to the flexibility of pure HDPE, making it a highly competitive solution for micro-hydropower energy production.

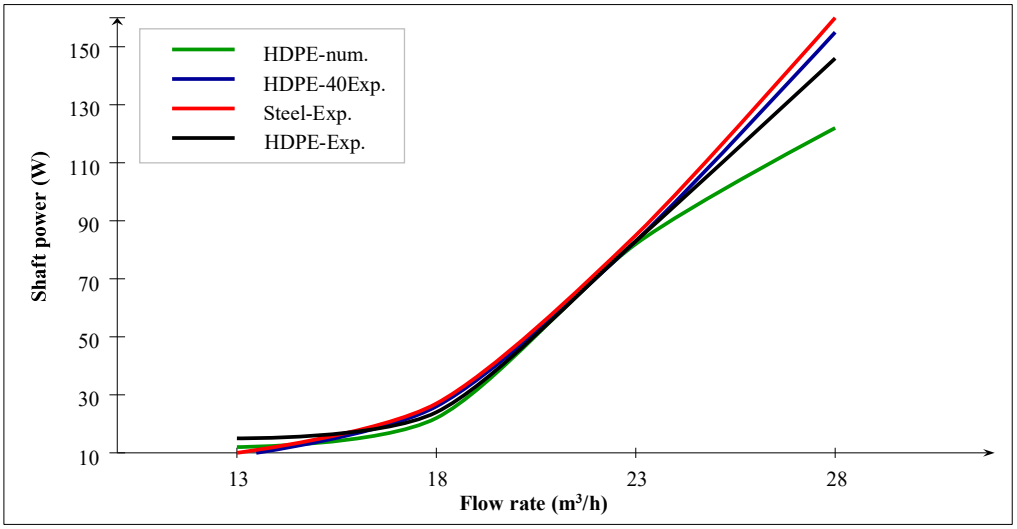


**Figure 11. Comparison of mechanical shaft power output as a function of flow rate for Steel, Pure HDPE and HDPE-40% Wood runners**

Figure 12 quantitatively presents the maximum equivalent von Mises stress recorded on the blades across the tested flow range (13-28 m³/h). A clear distinction emerges between the materials. The Pure HDPE runner exhibits lower stress levels, peaking at approximately 9 MPa. However, this lower stress value is misleading: it results directly from the material's low stiffness, which allows the blades to deform excessively under load (in Figure 6) rather than resisting the hydrodynamic pressure.

The HDPE-40% Wood runner displays higher stress levels, reaching a maximum of 14.64 MPa at the highest flow rate (28 m³/h). This increase is physically consistent with the enhanced stiffness of the biocomposite: the reinforced blades oppose the fluid forces more effectively, generating higher internal reaction stresses. Crucially, despite this increase, the maximum stress of 14.64 MPa remains far below the biocomposite's yield strength of 41.72 MPa. This corresponds to a minimum safety factor of 2.85 under the most severe operating conditions, confirming that the HDPE-40% wood material maintains structural integrity without risking plastic deformation or failure.

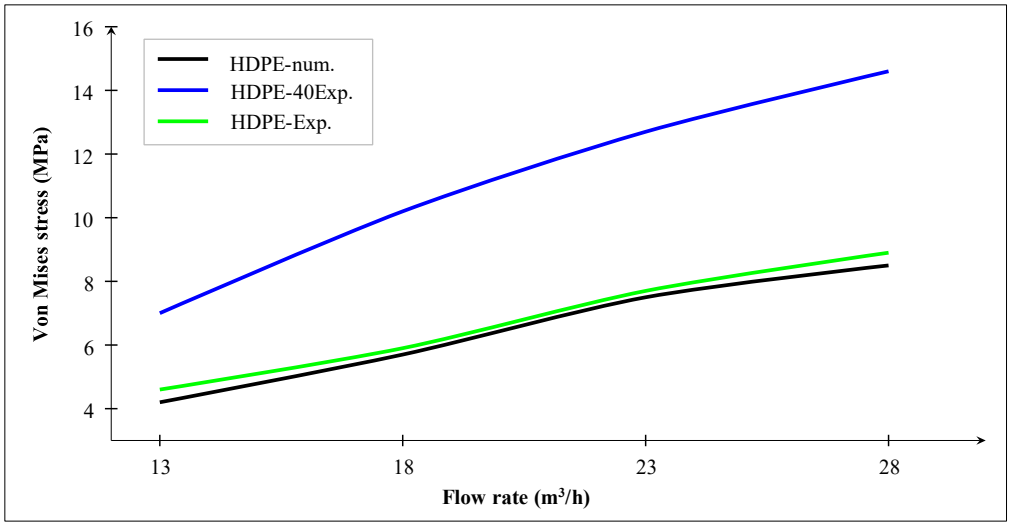


**Figure 12. Evolution of maximum von Mises stress as a function of flow rate for Pure HDPE (numerical/experimental) and HDPE-40% Wood composite runners**

Figure 13 illustrates the magnitude of the resultant radial force acting on the turbine shaft across the operating flow range. As expected, hydrodynamic loads increase monotonically with flow rate for all configurations. A clear distinction emerges between the materials: The HDPE-40% Wood runner sustains the highest radial forces, reaching approximately 4 kN at maximum flow. This elevated load directly reflects the superior structural stiffness of the biocomposite. Because the blades maintain their intended geometry without excessive bending, they intercept the full momentum of the water

jet, resulting in a larger reaction force transmitted to the shaft. Conversely, the Pure HDPE runner experiences significantly lower radial forces, peaking around: 3.2-3.4 kN. This reduction does not indicate improved hydrodynamics; rather, it stems from the fluid-structure interaction described in Figure 6. As the flexible HDPE blades deform and yield under water pressure, they shed part of the hydrodynamic load, leading to reduced energy transfer and the lower efficiency observed in Figure 8. Overall, the higher radial forces measured on the biocomposite runner provide positive confirmation of its ability to maintain hydrodynamic performance under load, consistent with the robust safety factors established in the structural analysis.

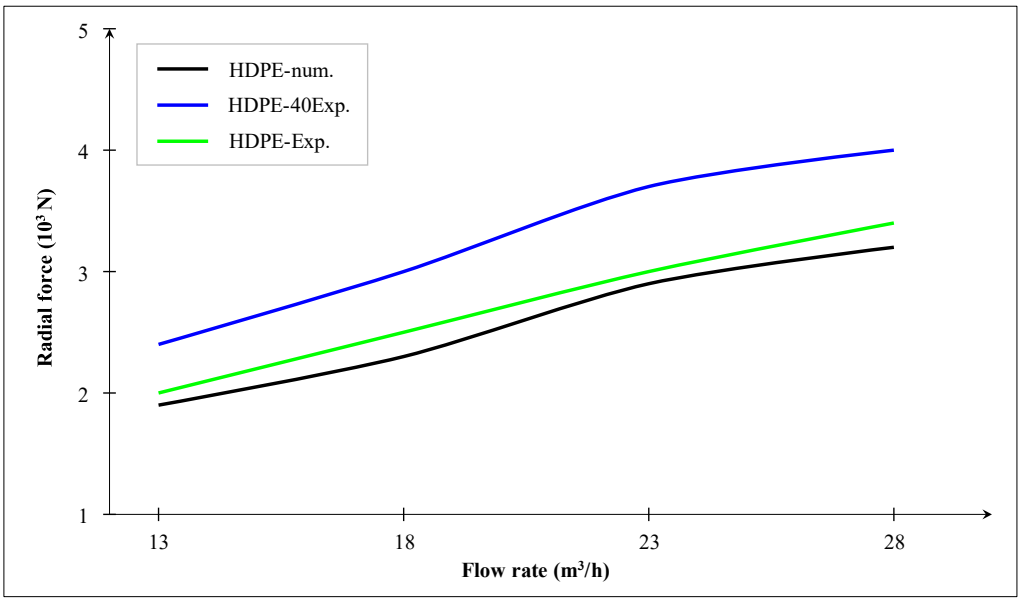


**Figure 13. Comparative evolution of radial forces acting on the runner shaft as a function of flow rate for Pure HDPE and HDPE-40% Wood runners**

Figure 14 presents the variation of the axial force acting along the runner shaft. Although Cross-flow turbines are primarily subjected to radial loading, evaluating the axial component remains essential for proper bearing selection and mechanical sizing. The results show a linear increase in axial thrust with flow rate for all materials. The HDPE-40% Wood runner exhibits a slightly higher axial load than the Pure HDPE configurations, reaching approximately 0.24 kN at 28 $m^3$/h. This marginal increase is attributed to the inherent surface roughness of the biocomposite and the slight thickness variations associated with the thermoforming process, which can induce minor asymmetric flow patterns. Importantly, the magnitude of this load remains very small: the maximum axial force (~ 0.24 kN) is roughly 16 times lower than the maximum radial force (~ 4kN) reported in Figure 12. Consequently, the axial thrust generated by the biocomposite runner is negligible relative to the turbine's overall loading and remains well within the capacity of standard (roller) bearings, ensuring no adverse impact on mechanical lifespan.

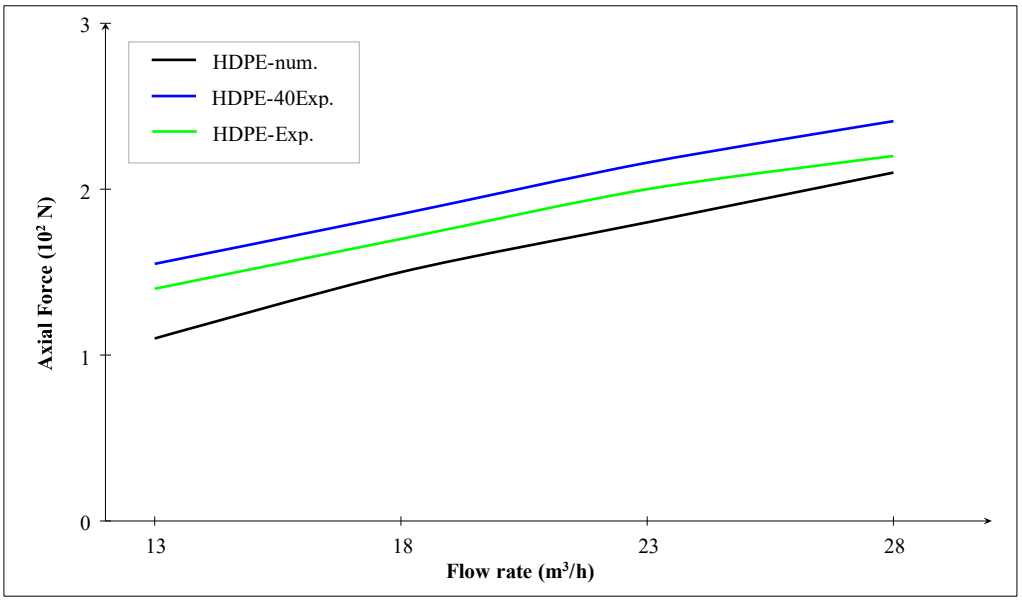


**Figure 14. Comparative evolution of axial thrust on the turbine shaft as a function of flow rate for Pure HDPE and HDPE-40% Wood runners**

Figure 15 provides a direct comparison of the structural deflection (maximum total deformation) experienced by the turbine blades under hydraulic load. The results highlight the most significant mechanical advantage of the biocomposite material. The Pure HDPE runner exhibits substantial deformation, increasing linearly with flow rate and reaching a maximum of approximately (0.16 mm). This confirms the inherent flexibility of the pure polymer, which leads to the "hydroelastic" efficiency losses discussed in previous sections. In sharp contrast, the HDPE-40% Wood runner demonstrates markedly superior rigidity. The maximum deformation is limited to only (0.042 mm) at the highest flow rate. This corresponds to a reduction of approximately 74% compared with the Pure HDPE runner. This dramatic improvement confirms that the 40% wood‑fiber reinforcement effectively compensates for the low stiffness of the thermoplastic matrix, ensuring that the blade profile remains geometrically stable and hydrodynamically efficient even under peak operating loads.

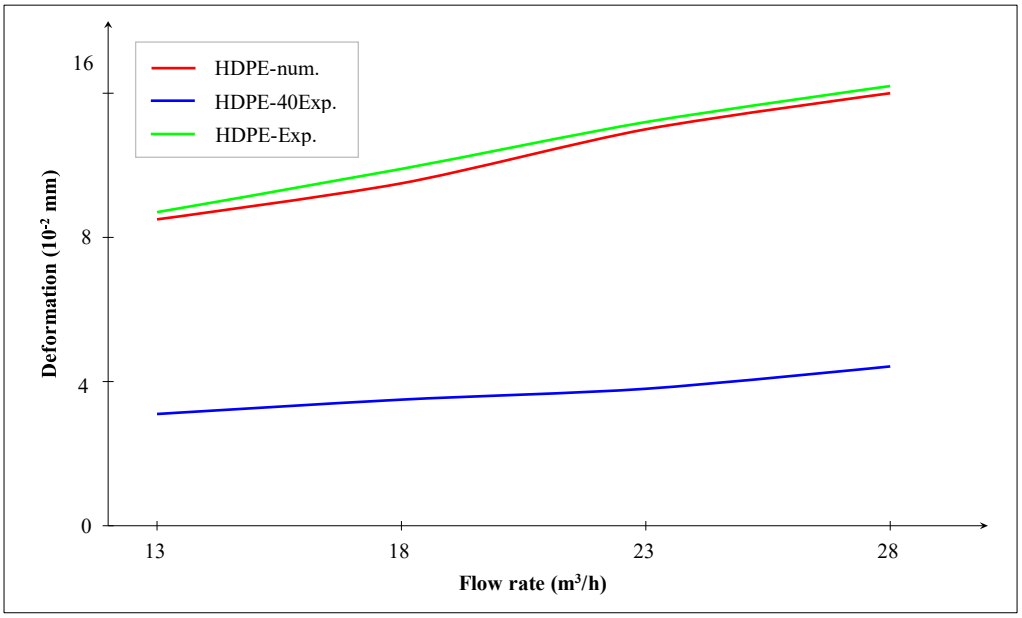


**Figure 15. Comparative evolution of maximum blade deformation as a function of flow rate for Pure HDPE (numerical/experimental) and HDPE-40% Wood biocomposite runners**

## 8. Conclusion

Conclusion This study presented a comprehensive numerical and experimental investigation of a Cross-flow turbine runner manufactured from recycled HDPE reinforced with 40% wood fibers. By integrating CAD-based geometric modeling, thermoforming fabrication, CFD hydrodynamic simulations, and FEA structural analysis within a calibrated and experimentally validated framework, the work provides a robust multiphysics assessment of the biocomposite runner's performance relative to steel and pure HDPE alternatives. The strong agreement between numerical predictions and experimental measurements confirms the reliability of the adopted methodology and strengthens confidence in the predictive modeling approach.

The hydrodynamic results demonstrate that the HDPE-40% wood runner maintains stable jet–blade interaction during both energy-transfer stages of the Cross-flow turbine. The increased stiffness provided by the wood fibers effectively limits hydroelastic deformation, ensuring that the designed inlet and outlet blade angles are preserved under operating conditions. Consequently, the biocomposite runner achieves 87-92% of the hydraulic efficiency of the steel runner, despite its significantly lower density and elastic modulus. This performance confirms that geometric fidelity and effective momentum exchange can be maintained using reinforced thermoplastic materials.

Structurally, the biocomposite runner exhibits a maximum deformation of only 0.042 mm and a peak von Mises stress of 14.64 MPa, corresponding to a safety factor of 2.85 relative to the material's yield strength. These results demonstrate that the reinforced HDPE matrix provides sufficient rigidity and load-bearing capacity to withstand combined hydrodynamic and centrifugal forces without compromising dimensional stability. Overall, the findings establish high-fraction wood-fiber biocomposites as technically viable, sustainable, and economically competitive alternatives to metallic runners for decentralized micro-hydropower systems. Future research will focus on long-term durability, fatigue behavior, moisture effects, and anisotropic material modeling to further enhance predictive accuracy and expand the application of biocomposite turbine components.

## 9. Declarations

### 9.1. Author Contributions

Conceptualization, F.M.K., G.D.N., and F.E.; methodology, F.M.K.; software, F.M.K.; validation, F.M.K., G.D.N., and T.M.T.; formal analysis, F.M.K. and T.M.T.; investigation, F.M.K.; resources, G.D.N. and F.E.; data curation, F.M.K.; writing—original draft preparation, F.M.K.; writing—review and editing, G.D.N., F.E., and T.M.T.; visualization, F.M.K.; supervision, G.D.N. and F.E.; project administration, G.D.N. and F.E. All authors have read and agreed to the published version of the manuscript.

### 9.2. Data Availability Statement

The data presented in this study are available on request from the corresponding author.

### 9.3. Funding

The authors received no financial support for the research, authorship, and/or publication of this article.

### 9.4. Acknowledgments

The authors extend their sincere gratitude to the Laboratory of Turbomachines, the Laboratory of Bioplastics and Nanotechnology, and the Laboratory of Biomaterials at UQAT for their invaluable technical and logistical support.

### 9.5. Institutional Review Board Statement

Not applicable.

### 9.6. Informed Consent Statement

Not applicable.

### 9.7. Declaration of Competing Interest

The authors declare that they have no known competing financial interests or personal relationships that could have appeared to influence the work reported in this paper.

## 10. References

[1] Paish, O. (2002). Small hydro power: Technology and current status. Renewable and Sustainable Energy Reviews, 6(6), 537–556. doi:10.1016/S1364-0321(02)00006-0.

[2] Sen, R., & Bhattacharyya, S. C. (2014). Off-grid electricity generation with renewable energy technologies in India: An application of HOMER. Renewable Energy, 62, 388–398. doi:10.1016/j.renene.2013.07.028.

[3] Harvey, A., Brown, A., Hettiarachi, P., & Inversin, A. (1993). Micro-hydro Design Manual: A guide to small-scale water power schemes. Intermediate Technology Publications, London, United Kingdom.

[4] Anand, R. S., Jawahar, C. P., Bellos, E., & Malmquist, A. (2021). A comprehensive review on Crossflow turbine for hydropower applications. Ocean Engineering, 240, 110015. doi:10.1016/j.oceaneng.2021.110015.

[5] Elbatran, A. H., Yaakob, O. B., Ahmed, Y. M., & Shabara, H. M. (2015). Operation, performance and economic analysis of low head micro-hydropower turbines for rural and remote areas: A review. Renewable and Sustainable Energy Reviews, 43, 40–50. doi:10.1016/j.rser.2014.11.045.

[6] Assefa, E. Y., & Tesfay, A. H. (2025). Effect of Blade Profile on Flow Characteristics and Efficiency of Cross-Flow Turbines. Energies, 18(12), 3203. doi:10.3390/en18123203.

[7] Harefa, P., Bramantya, M. A., & Waluyo, J. (2025). Numerical Simulation of the Effect of Number of Runner Blades on a Cross-Flow Turbine Performance. Proceedings of the International Conference on Science and Technology, 11–25. doi:10.2991/978-94-6463-772-4_3.

[8] Hunt, A., Talpey, G., & Polagye, B. Experimental evaluation of advanced control strategies for high-blockage Cross-flow turbine arrays. doi:10.48550/arXiv.2507.02194.

[9] Faruk, O., Bledzki, A. K., Fink, H. P., & Sain, M. (2012). Biocomposites reinforced with natural fibers: 2000-2010. Progress in Polymer Science, 37(11), 1552–1596. doi:10.1016/j.progpolymsci.2012.04.003.

[10] Pickering, K. L., Efendy, M. G. A., & Le, T. M. (2016). A review of recent developments in natural fibre composites and their mechanical performance. Composites Part A: Applied Science and Manufacturing, 83, 98–112. doi:10.1016/j.compositesa.2015.08.038.

[11] Kifumbi, F. M., Ngoma, G. D., Erchiqui, F., & Tshibangu, T. M. (2025). Experimental and Numerical Modeling of a Cross-Flow Turbine Runner Made of HDPE: Experimental and Numerical Approach. HighTech and Innovation Journal, 6(4), 1104–1122. doi:10.28991/hij-2025-06-04-01.

[12] Ahmad, H., & Rodrigue, D. (2025). Mechanical Recycling of Crosslinked High-Density Polyethylene (xHDPE). Processes, 13(3), 809. doi:10.3390/pr13030809.

[13] MachineMFG. (2026). Polypropylene vs. HDPE: Material differences and comparisons. MachineMFG, United States. Available online: https://shop.machinemfg.com/polypropylene-vs-hdpe-material-differences-and-comparisons/ (accessed on May 2026).

[14] Adhikari, R., & Wood, D. (2018). The design of high efficiency crossflow hydro turbines: A review and extension. Energies, 11(2), 267. doi:10.3390/en11020267.

[15] Koffi, A., Mijiyawa, F., Koffi, D., Erchiqui, F., & Toubal, L. (2021). Mechanical properties,wettability and thermal degradation of HDPE/birch fiber composite. Polymers, 13(9), 1459. doi:10.3390/polym13091459.

[16] Basiji, F., Erchiqui, F., Koubaa, A., & Ghasemi, I. (2025). Influence of fiber concentration and length on the dielectric, mechanical, and thermal properties of maple wood fiber-reinforced polypropylene. Journal of Thermoplastic Composite Materials. doi:10.1177/08927057251319772.

[17] Mijiyawa, F. (2018). Formulation, caractérisation, modélisation et prévision du comportement thermomécanique des pièces plastiques et composites de fibres de bois: application aux engrenages. Doctoral dissertation, Université du Québec à Trois-Rivières, Québec, Canada.

[18] Quaranta, E., Perrier, J. P., & Revelli, R. (2022). Optimal design process of crossflow Banki turbines: Literature review and novel expeditious equations. Ocean Engineering, 257, 111582. doi:10.1016/j.oceaneng.2022.111582.

[19] Galvis-Holguin, S., Rio, J. S. Del, González-Arango, D. I., Correa-Quintana, E., & Meneses, L. D. R. (2025). Numerical and Experimental Validation of a New Methodology for the Design of Michel-Banki Turbine. CFD Letters, 17(5), 76–89. doi:10.37934/cfdl.17.5.7689.

[20] Prasad, L. B. (2025). Dynamic modelling and response of a Cross-flow turbine runner. Doctoral dissertation, Pulchowk Campus, Patan, Nepal.

[21] Mockmore, C. A., & Merryfield, F. (1949). The Banki Water Turbine. Engineering Experiment Station, Oregon State College, Corvallis, Bulletin Series No. 25, Oregon, United States.

[22] Sammartano, V., Aricò, C., Carravetta, A., Fecarotta, O., & Tucciarelli, T. (2013). Banki-Michell optimal design by computational fluid dynamics testing and hydrodynamic analysis. Energies, 6(5), 2362–2385. doi:10.3390/en6052362.

[23] Aziz, N. M., & Totapally, H. G. S. (1994). Design Parameter refinement for improved Cross-Flow turbine performance: Engineering Report. Clemson University, South Carolina, United States.

[24] López-Pachón, M., & Marcé-Nogué, J. (2025). The crucial role of meshing in computational fluid dynamics simulations for organic geometries in paleobiology: Describing fluid dynamics performance through best practices. Methods in Ecology and Evolution, 16(10), 2170–2194. doi:10.1111/2041-210X.70146.

[25] Kurowski, P. M. (2019). Engineering Analysis with SolidWorks Simulation 2019. SDC Publications, Kansas, United States.

[26] Gairola, S. P., Tyagi, Y., & Gupta, N. (2022). Mechanical Properties Evaluation of Banana Fibre Reinforced Polymer Composites: a Review. Acta Innovations, 2022(42), 59–70. doi:10.32933/ActaInnovations.42.5.

[27] Ji, Y., Song, H., Xue, Z., Li, Z., Tong, M., & Li, H. (2023). A Review of the Efficiency Improvement of Hydraulic Turbines in Energy Recovery. Processes, 11(6), 163–172. doi:10.3390/prl1061815.

[28] Jalaee, A., Trottman, K., French, V., Raghunath, S., Brito dos Santos, F., & Foster, E. J. (2024). Improved thermomechanical and rheological properties of polypropylene composites with thermomechanical pulp for injection molding. Polymer Composites, 45(14), 12782–12795. doi:10.1002/pc.28667.